Journal of Power Sources 206 (2012) 469–475

Contents lists available at SciVerse ScienceDirect

Journal of Power Sources

journal homepage: www.elsevier.com/locate/jpowsour

Designing tunable microstructures of Mn_3O_4 nanoparticles by using surfactant-assisted dispersion

Ying-Feng Lee, Kuo-Hsin Chang, Chi-Chang Hu*, Yi-Hsuan Chu

Laboratory of Electrochemistry and Advanced Materials, Department of Chemical Engineering, National Tsing-Hua University, No. 101, Section 2, Kuang-Fu Road, Hsin-Chu 30013, Taiwan

ARTICLE INFO

Article history:
Received 8 September 2011
Received in revised form 12 January 2012
Accepted 20 January 2012
Available online 28 January 2012

Keywords:
Manganese oxide
Copolymer
Surfactant
Supercapacitor
High-power

ABSTRACT

Porous Mn_3O_4 nanoparticles with tunable microstructures are synthesized from $Mn(AcO)_2{\cdot}4H_2O$ with Pluronic F127 as a dispersant. The amount of copolymer served as the surfactant in the precursor solution is varied to change/tune the specific surface area/porosity of Mn_3O_4. The textural and electrochemical properties of porous Mn_3O_4 nanoparticle are systematically characterized by means of the N_2 adsorption/desorption isotherms, scanning electron microscopic (SEM), transmission electron microscopic (TEM), X-ray diffraction (XRD), and voltammetric analyses. The interactions between manganese precursor and triblock copolymer can be used to control the microstructures of resultant oxides. Mn_3O_4 nanoparticles with tunable porosity and high surface area achieve the excellent capacitive performances (e.g., high-power characteristics and impressive capacitance retention) for next generation supercapacitors. The specific surface area indicating the electrochemically active sites for charge storage/delivery as well as the pore structure indexed by the BJH pore volume, which affects the ion transportation and electrolyte permeation, have been demonstrated to be the key factors determining the capacitive performances of Mn_3O_4 in the low-rate and high-rate processes, respectively.

1. Introduction

Dispersion and self-assembly of block copolymers, surfactants, colloidal suspensions, and proteins provide a versatile approach to create unique nanostructures of compounds with potential applications in biomedicines, optoelectronics, energy storage and conversion technology, etc. [1–13]. In the past two decades, several block copolymers, such as F127 ($EO_{106}PO_{70}EO_{106}$), P123 ($EO_{20}PO_{70}EO_{20}$), and $EO_{75}PO_{45}$ have been used to facilitate the dispersion/self-assembly process in forming various nanostructures and controlling the size and morphology of oxide materials [5,6]. Recently, we successfully carbonized the self-assembled polymer to inhibit the grain growth and aggregation of anatase TiO_2 nanocrystals, which can be further reduced in the crystal size by increasing the polymer/Ti ratio in preparing the precursor mixture [14]. Moreover, a 3-D mesoporous, well crystalline RuO_2 film was prepared via the evaporation-induced self-assembled (EISA) method, which successfully demonstrated the extremely high power performances (e.g., excellent capacitive behavior at 10,000 mV s^{-1} and ultrahigh-frequency capacitive responses) [15]. Accordingly, this dispersion/self-assembly method is a powerful route in synthesizing and functioning nanomaterials for many important applications.

Manganese oxides have attracted considerable research interest due to their promising application potentials in several fields, e.g., catalysis [16,17], ion exchange [18,19], molecular adsorption [20,21], magnetic applications [22,23], secondary batteries [24,25], and supercapacitors [26–28]. For instance, Mn_3O_4 has been used as an active catalyst for decomposing NO_x produced from internal engines and oxidizing benzene or carbon monoxide [16,17,29]. In addition, this oxide was reported to be a promising material in electrochromic applications [30]. On the other hand, MnO_x is widely reported to be a promising electrode material in both alkaline batteries and electrochemical supercapacitors [26–28,31], which undergoes redox transitions between different oxidation states to store and deliver electric energy. All of the above reports reveal the great interest in synthesizing manganese oxides in various forms/structures for a wide variety of applications.

On the basis of the above application potentials, there are many studies trying to synthesize manganese oxides of desired architecture in order to achieve ideal functions in their unique applications, e.g., calcinations of MnO_2 and Mn_2O_3, surfactant-assisted or ultrasonic-assisted hydrothermal synthesis, chemical bath deposition, sol–gel synthesis, co-precipitation, electrochemical deposition, etc. [26,28,32–36]. Very recently, in order to tackle global warming, mesoporous MnO_x has been considered as

* Corresponding author. Tel.: +886 3 573 6027; fax: +886 3 573 6027.
E-mail address: cchu@che.nthu.edu.tw (C.-C. Hu).

0378-7753/$ – see front matter © 2012 Elsevier B.V. All rights reserved.
doi:10.1016/j.jpowsour.2012.01.121

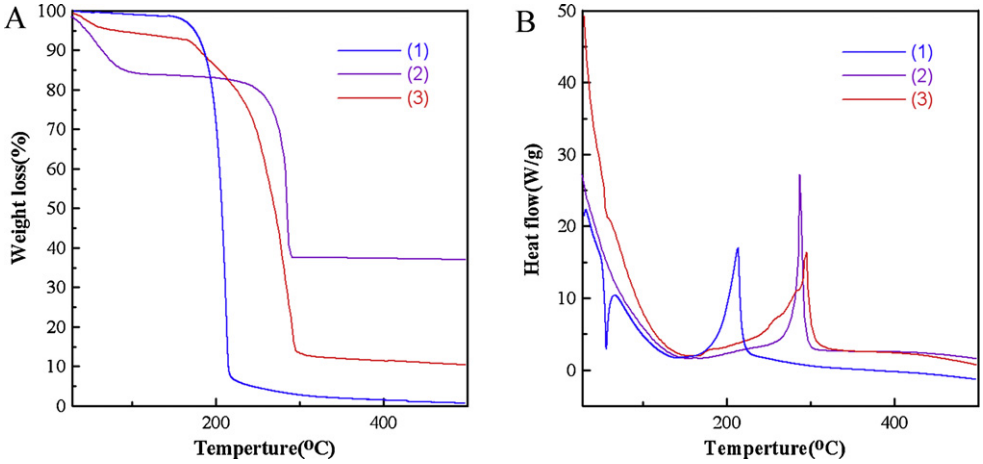

Fig. 1. (A) TGA and (B) DTA curves measured under an air flow at 5 °C min^{-1} from room temperature to 500 °C for (1) block copolymer (F127), (2) manganese acetate, and (3) the dried precursor mixture for preparing Mn_3O_4-L.

potential candidates for the electrode materials of rechargeable Li-ion batteries and supercapacitors [37–39]. However, crystalline Mn_3O_4 without electrochemical activation showed lower specific capacitance and poor capacitance retention [40]. On the other hand, MnO_x electrochemically activated from Mn_3O_4 and the Mn-based oxide composites generally showed excellent cycle stability and fairly high specific capacitance [41,42]. Therefore, how to get large amount of porous MnO_x with high specific surface area and desired microstructures for various applications is still a challenge. Here, porous Mn_3O_4 nanoparticles with tunable microstructures were proposed to be synthesized through the usage of a block copolymer template (Pluronic F127) as a dispersant. The amount of copolymer served as the surfactant in the precursor solution was varied to change/tune the specific surface area/porosity of resultant Mn_3O_4 fabricated by a thermal decomposition procedure in the gram scale production. The textural and capacitive properties of porous Mn_3O_4 nanoparticle were systematically characterized by means of the N_2 adsorption/desorption isotherms, scanning electron microscopic (SEM), transmission electron microscopic (TEM), X-ray diffraction (XRD), and voltammetric analyses. Finally, how to tune the nanostructure of porous Mn_3O_4 and the complicated interactions between manganese precursor and triblock copolymer during the reaction are discussed, which is applicable to the synthesis of other nanostructured oxides.

2. Experimental

2.1. Preparation of porous Mn_3O_4 nanoparticles and electrode preparation

Pluronic F127 ($EO_{106}PO_{70}EO_{106}$) was dissolved in methanol and manganese acetate serving as the manganese precursor was added into the above solution under stirring for about 2 h. The mixtures were heated under an air flow at a ramping rate of 1 °C min^{-1} to 300 °C and then cooled down to room temperature. In this work, three samples with varying the molar ratio of Mn^{2+}/F127 from 1/0.016, 1/0.064, and 1/0.08 were prepared and the resultant Mn oxides are denoted as Mn_3O_4-L, Mn_3O_4-M and Mn_3O_4-H, respectively. The detailed composition of the precursor mixtures is listed in Table 1. The oxide powders were mixed with poly (vinylidene difluoride) powders and then N-methylpyrolidinone (NMP, ISP) solvent was added to form a solution. The mixed solution was dipped onto graphite substrates and finally, the electrodes were dried in an oven for 8 h at 85 °C. The loading mass of Mn_3O_4 nanoparticles powder is between 0.5 and 0.75 mg cm^{-2}. The electrodes were coated with PTFE films with an exposed area of 1 cm^2 for electrochemical characterization.

2.2. Characterization

The weight loss and thermal data of the dried mixture during the oxide formation process were measured by the thermogravimetric/differential thermal analyses (TG/DTA, TA Instruments SDT Q600) under an air flow at 5 °C min^{-1} from room temperature to 500 °C. The XRD patterns of all samples were recorded with an X-ray powder diffractometer (CuKα, Ultima IV, Rigaku) at an angular rate of 1° min^{-1} (2θ). The crystal size of Mn_3O_4 was estimated with the Debye–Scherrer equation from face (2 1 1) of Mn_3O_4. The specific surface area and average BJH pore size were obtained from the N_2 adsorption/desorption analyses at 77 K (Nova-1200e, Quantachrome). The BET specific surface area was calculated from the adsorption isotherms at the relative pressure range from 0.1 to 0.3, meanwhile the BJH pore size distribution was determined from the desorption isotherms. The morphologies and microstructures of oxides were characterized by transmission electron microscopy (TEM) using a JEOL 2100. The field-emission scanning electron microscopic (FE-SEM) observations were performed on a JEOL JSM-6700F with an accelerating voltage of 3.0 keV. Electrochemical characteristics of porous Mn_3O_4-coated electrodes were examined by means of an electrochemical analyzer system, CHI 633C (CH Instruments, USA) in a three-compartment cell. The electrolyte, not specified in this work, is 0.5 M Na_2SO_4. An Ag/AgCl electrode (Argenthal, 3 M KCl, 0.207 V vs. SHE at 25 °C) was used as the reference and a piece of platinum gauze was employed as the counter electrode.

3. Results and discussion

3.1. Characterization of precursors

TG/DTA analyses of Pluronic F127, manganese acetate, and the aged mixture for preparing Mn_3O_4-L under an air flow were used to gain the information for determining the suitable thermal decomposition temperature in air and typical results are shown in Fig. 1. From curve 1 in Fig. 1, the very sharp weight loss accompanying an exothermic peak between ca. 160 and 230 °C is reasonably attributed to the combustion of Pluronic F127. On the other hand, the gradual weight loss from room temperature to ca. 100 °C on curve 2 indicates the evaporation of physically adsorbed water molecules of $Mn(AcO)_2{\cdot}4H_2O$. The obvious weight loss between

Table 1
The average crystal size and physical properties of porous Mn_3O_4 nanoparticles.

Sample	Mn_3O_4-L	Mn_3O_4-M	Mn_3O_4-H
Molar ratio[a]	1:0.016:49.5:5.6	1:0.064:49.5:5.6	1:0.08:49.5:5.6
BET specific surface area, $m^2\ g^{-1}$	48	84	102
Total pore volume, $cm^3\ g^{-1}$	0.428	0.280	0.242
Average pore diameter, nm	3.607	3.842	3.882
Average crystal size, nm[b]	14.8	11.4	11.7

[a] Represent the molar ratio of manganese acetate:F127:methanol:water.
[b] Based on the XRD peak corresponding to facet (2 1 1) and the Debye–Scherrer equation.

240 and 290 °C results from the rapid decomposition of the acetate compound. Consequently, the result of the mixture for preparing Mn_3O_4-L on curve 3 displays combined characteristics of curves 1 and 2. The above phenomenon indicates that the copolymer combustion started at 180 °C to release extensive gases for generating large pores of the resultant oxide and then, the acetate species will decompose at 240 °C to provide the small pore structure due to the extensive evolution of carbon dioxide and water (steam). The strategy of this two-step combustion provided an efficient route to enhance the porosity and surface area of resultant oxides. Eventually, fine-tuning the porosity and designing the nanostructure of Mn_3O_4 can be achieved by varying the amount of Pluronic F127.

Fig. 2 shows the importance of using the acetate precursor. Curve 1 shows the typical XRD pattern corresponding to the $Mn(AcO)_2{\cdot}4H_2O$ crystals. In comparing with pattern 1, pattern 2 shows an amorphous structure for the precursor derived from $Mn(AcO)_2{\cdot}4H_2O$, indicating occurrence of transformation of Mn^{2+} in methanol when $Mn(AcO)_2{\cdot}4H_2O$ was dissolved in the methanol solution. Moreover, this amorphous Mn precursor can be decomposed in air at/below 300 °C to form Mn_3O_4 crystals from the TGA-DTA analysis. From pattern 3, on the other hand, the above transformation of Mn salts did not occur when $MnCl_2{\cdot}4H_2O$ was dissolved in methanol. As a result, this salt kept its original crystalline structure when solvent was evaporated completely. Since $MnCl_2{\cdot}4H_2O$ does not decompose at 300 °C under an air flow, Mn_3O_4 cannot be obtained at such a relatively low temperature. Similar results are obtained for $MnSO_4{\cdot}H_2O$ and $Mn(NO_3)_2{\cdot}6H_2O$ (not shown here), revealing the importance of using the acetate precursor. A comparison of the UV–vis spectra between $Mn(AcO)_2{\cdot}4H_2O$ (Fig. S1-A) and $MnCl_2{\cdot}4H_2O$ (Fig. S1-B) dissolved in methanol clearly points out the obvious color change during the transformation in the $Mn(AcO)_2{\cdot}4H_2O$ solution, further supporting the above statements.

3.2. Synthesis and characterization of Mn_3O_4

The effects of varying the amount of Pluronic F127 on the crystal size and microstructure of Mn_3O_4 particulates were examined by the X-ray diffraction (XRD) analysis and the results are shown in Fig. 3. Clearly, all XRD patterns reveal the formation of Hausmannite Mn_3O_4 (in comparing with the PDF 80-0382 file). However, the formation of Mn_3O_4 is only successful when manganese acetate is employed as the precursor because the other precursors such as $MnCl_2{\cdot}4H_2O$, $MnSO_4{\cdot}H_2O$, and $Mn(NO_3)_2{\cdot}6H_2O$ do not generate the Mn_3O_4 crystals (see Fig. S2). This phenomenon is due to the formation of an amorphous organic Mn precursor and that $Mn(AcO)_2{\cdot}4H_2O$ is more easily oxidized in comparison with the above inorganic precursors [43]. The Debye–Scherrer equation was used to estimate the average crystal size. Based on face (2 2 1), the average crystal size of Mn_3O_4-L (14.7 nm) is obviously larger than that of the other two samples (11.4 and 11.7 nm for Mn_3O_4-M and Mn_3O_4-H, respectively). The diffraction peaks become broader with increasing the content of Pluronic F127, revealing the successful control of the Mn_3O_4 crystal size.

The scanning electron microscopic (SEM) analysis clearly shows the significant difference in the morphology of Mn_3O_4 with varying the copolymer amount. In Fig. 4A, Mn_3O_4-L shows an aggregated plate morphology which means a limited suspension degree of the precursor nanoparticles. Accordingly, large pore but small specific surface area is obtained (see below). By increasing the amount of copolymer, Mn_3O_4-M in Fig. 4B shows the nanosphere-like morphology. This result suggests that the distribution of precursor particles are enhanced but the amount of copolymer is not enough to separate each precursor particulate. Eventually, with the highest amount of Pluronic F127 in this work, Mn_3O_4-H in Fig. 4C shows the well-distributed nanoparticles and exhibits the highest surface

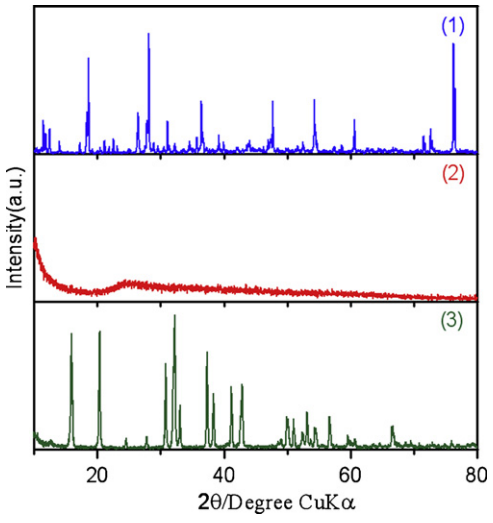

Fig. 2. Powder XRD patterns of (1) $Mn(AcO)_2{\cdot}4H_2O$ and (2,3) the dried precursors from the methanol solution containing (2) $Mn(AcO)_2{\cdot}4H_2O$ and (3) $MnCl_2{\cdot}4H_2O$.

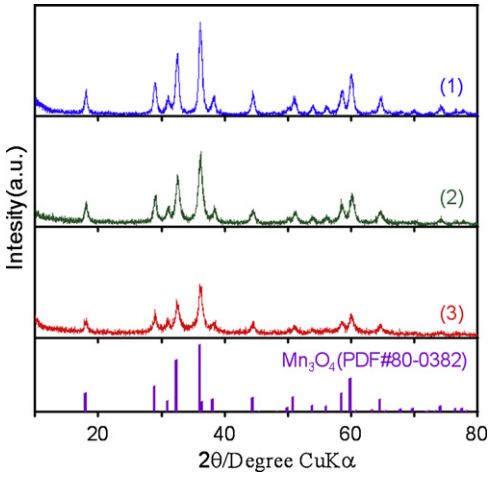

Fig. 3. Powder XRD patterns of (1) Mn_3O_4-L, (2) Mn_3O_4-M, and (3) Mn_3O_4-H.

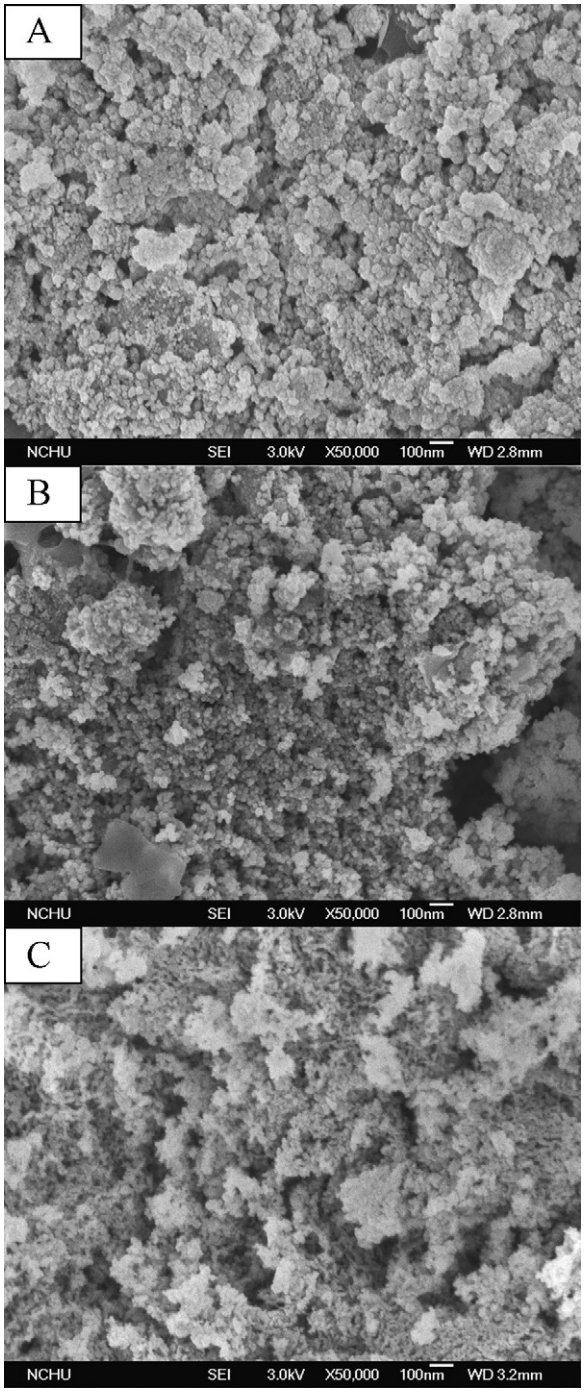

Fig. 4. SEM images of (A) Mn_3O_4-L, (B) Mn_3O_4-M, and (C) Mn_3O_4-H.

area among all samples (see below), suggesting that the amount of copolymer is high enough to separate each precursor nanoparticles.

To further confirm the variation in the morphologies of porous Mn_3O_4 nanoparticles, all samples were examined by the transmission electron microscopic (TEM) analysis and typical results are shown in Fig. 5. Clearly, Mn_3O_4-L shows the formation of large Mn_3O_4 aggregates resulting from the relatively poor dispersion of manganese acetate molecules due to the low content of Pluronic F127. However, Mn_3O_4-M and Mn_3O_4-H show the nanosphere-like morphology, indicating the effective formation and suspension of precursor particles during the reaction. Since the particulate size and the size distribution of Mn_3O_4-H are smaller and more uniform than that of Mn_3O_4-M, the formation of precursor nanoparticles during the dried period are more efficient for preparing Mn_3O_4-H because of enough Pluronic F127. All the above results clearly demonstrate the success in synthesizing highly uniform-distributed nanoparticles by varying the amount of Pluronic F127, the surfactant.

The pore structure of oxides was examined by using the N_2 adsorption/desorption isotherms and typical results are shown in Fig. 6. All samples display the same hysteresis behavior in the relative pressure range from 0.4 to 1, indicating the same type (type IV) of pore structure. From an examination of Fig. 6 and the summarized data in Table 1, the following concept in the supercapacitor application has to be mentioned. Mn_3O_4-L and Mn_3O_4-M exhibit a broad pore distribution, including macroporous and mesoporous pores. This result indicates the formation of a hybrid pore structure in these oxides. The macroporous cores can provide large pores working as the ion-buffering reservoirs for the high-rate charging/discharging purpose. The mesopores generally provide the short ion-transport pathways and favor the direct contact of electrolytes to the electrochemically active sites, increasing the utilization of pseudocapacitance [44]. By tuning the amount of Pluronic F127 in the precursor media, Mn_3O_4-H possesses the wide pore size distribution and a relative high surface area among these oxides although its pore volume ($0.245\ cm^3\ g^{-1}$) is the smallest, attributable to the packed aggregates of Mn_3O_4 crystallites formed by thermal decomposition.

Based on all the above results and discussion, a synthesis scheme is proposed in Fig. 7 to illustrate the interactions between precursors and Pluronic F127 as well as to show how to form Mn_3O_4 nanoparticles. In preparing the precursor solution, homogeneously mixing $Mn(AcO)_2{\cdot}4H_2O$ and triblock copolymer is used to enhance the suspension of precursor nanoparticles. Note that transformation of $Mn(AcO)_2{\cdot}4H_2O$ does occur in the methanol solution, resulting in the formation of an amorphous Mn precursor when solvent has been evaporated. Meanwhile, due to the affinity of Mn ions to the hydrophilic part of Pluronic F127, the amorphous manganese precursors should be uniformly dispersed onto the polymer. Because of the well-distribution of Pluronic F127, the evaporation of solvent will lead to block the aggregation of Mn ions, favoring the suspension of precursor nanoparticles (step B). The polymers and Mn precursors in these surfactant-surrounded nanoparticles of amorphous Mn precursors will be decomposed through the so-called "two-step combustion" procedure (found in the TGA-DTA analysis shown in Fig. 1) in order to form Mn_3O_4 crystals (step C). Since the shape and suspension of Mn precursors strongly depend on the concentration of Pluronic F127, the porous architecture of Mn_3O_4 nanocrystals prepared by this thermal decomposition process is tunable through changing the surfactant concentration in the precursor mixture.

3.3. Capacitive performances of Mn_3O_4

The tunable porous structure of Mn_3O_4 nanoparticles in this work is very important to the electrochemical energy storage/conversion systems. Here, the pseudocapacitive behavior of various Mn_3O_4 is used to gain an understanding on the interactive influences between the specific surface area and pore volume of Mn_3O_4 and Fig. 8A–C show the typical cyclic voltamograms of Mn_3O_4-L, Mn_3O_4-M, and Mn_3O_4-H-coated electrodes in 0.5 M Na_2SO_4. Clearly, all *i–E* curves demonstrate a rectangle-like shape at/below $500\ mV\ s^{-1}$, which become relatively distorted when the scan rate reaches $2000\ mV\ s^{-1}$. This phenomenon may be due to the poor conductivity of Mn_3O_4 since no conductive carbons were mixed with Mn_3O_4 during the electrode preparation.

Fig. 8D shows the relationship between the specific capacitance and the scan rate of CV, which reveals the high capacitance retention and high-power performance of all Mn_3O_4-coated electrodes.

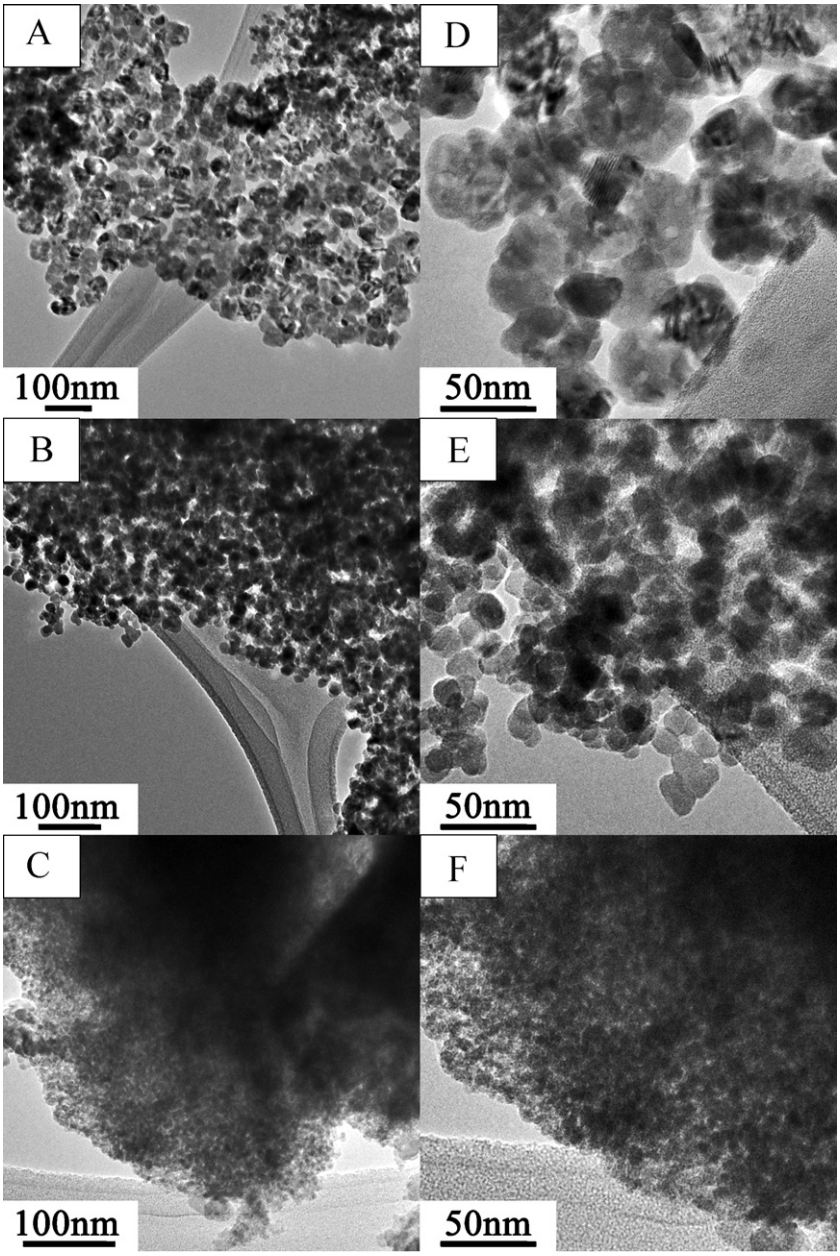

Fig. 5. TEM images of (A,D) Mn_3O_4-L, (B,E) Mn_3O_4-M, and (C,F) Mn_3O_4-H.

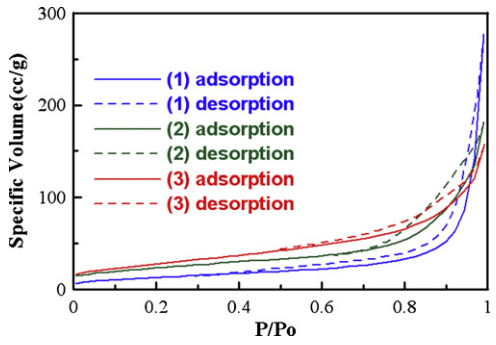

Fig. 6. N_2 adsorption/desorption isotherms of (1) Mn_3O_4-L, (2) Mn_3O_4-M, and (3) Mn_3O_4-H.

From an examination of Fig. 8D, the specific capacitance of Mn_3O_4 measured at low scan rates (e.g., <500 mV s^{-1}) is generally proportional to their specific surface area. The loss in the specific capacitance of all oxide-coated electrodes follows the same trend when the scan rate is below/equal to 500 mV s^{-1}, indicating that the electrolyte-accessible surface area decreases with increasing the scan rate of CV. On the other hand, the capacitance retention of the Mn_3O_4-M-coated electrode is the best among all Mn_3O_4-coated electrodes, especially at 2000 mV s^{-1}. This phenomenon is attributed to its smaller grain size (in comparison with Mn_3O_4-L) and larger specific pore volume (in comparison with Mn_3O_4-H) for the high-rate charging/discharging process. Clearly, Mn_3O_4-M with a lower specific surface area but a higher pore volume (in comparison with Mn_3O_4-H) shows a lower specific capacitance at slow scan rates (e.g., 5 mV s^{-1}) but a better capacitance retention at high scan rates (e.g., 2000 mV s^{-1}) due to the smooth supply of electrolytes from the ion-buffering reservoirs. This statement is further

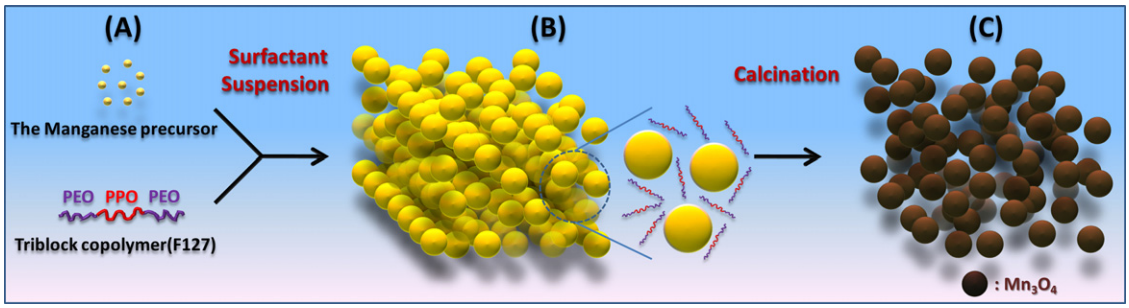

Fig. 7. The formation scheme of Mn_3O_4 nanocrystals through the thermal decomposition process; step (A): manganese acetate and triblock copolymer were dissolved in methanol; step (B): suspension of triblock copolymer and manganese acetate with phase transformation; step (C): formation of Mn_3O_4 nanoparticles under calcination.

supported by changing the concentration of the supporting electrolyte (see Fig. S3). The capacitance retention of Mn_3O_4-M becomes poor in the 0.1 M Na_2SO_4 solution when the scan rate is above 500 mV s^{-1} because the diluted ion-buffering reservoirs cannot supply enough ions to support the superficial redox reaction at extremely high charging/discharging rates.

The chronopotentiograms (CP) measured at different current densities were used to further characterize the charging/discharging behavior of Mn_3O_4 prepared in this work and typical results for Mn_3O_4-H are shown in Fig. 9. From curve 1 in Fig. 9A, the charge curve shows a relatively low slope in the potential range $\geq$ 0.6 V in comparison with its discharge counterpart, and hence, the discharging time is shorter than its corresponding charging time when the specific current (or current density based on mass) is equal to 2 A g^{-1}. This phenomenon is attributable to certain irreversible reactions, such as the oxidation of Mn_3O_4 into MnO_x and the dissolution of Mn_3O_4 in the charging process at potentials $\geq$ 0.6 V under low specific currents. As a result, the current efficiency of charge–discharge is low (about 70% at 2 A g^{-1}, see Fig. 9B). In fact, the transformation from Mn_3O_4 into MnO_x and the degradation mechanism of MnO_x-based electrode materials in neutral aqueous media have been reported previously [41,42,45,46]. The cycle stability of Mn oxides can be improved by lowering the upper potential limit of charge [42,45] or by adding some protective agents [46,47]. The transformation from Mn_3O_4 into MnO_x, i.e., electrochemical activation (sometimes even needs 2000 cycles), can enhance the resultant specific capacitance [41,42]. Since the faradaic charge-storage reaction of manganese species occurs at the superficial range of oxide under a high-rate operation, the above irreversible reactions become minor and negligible with increasing the specific current (see all CP curves in Fig. 9A). As a result, the CP curves become symmetric and the current efficiency of charge–discharge is improved to be equal to/above 95% when the specific current is equal to/larger than 16 A g^{-1}. Moreover, the current efficiency is 99% at 100 A g^{-1}, revealing the excellent power performance of Mn_3O_4-H, attributable to its highly porous nature.

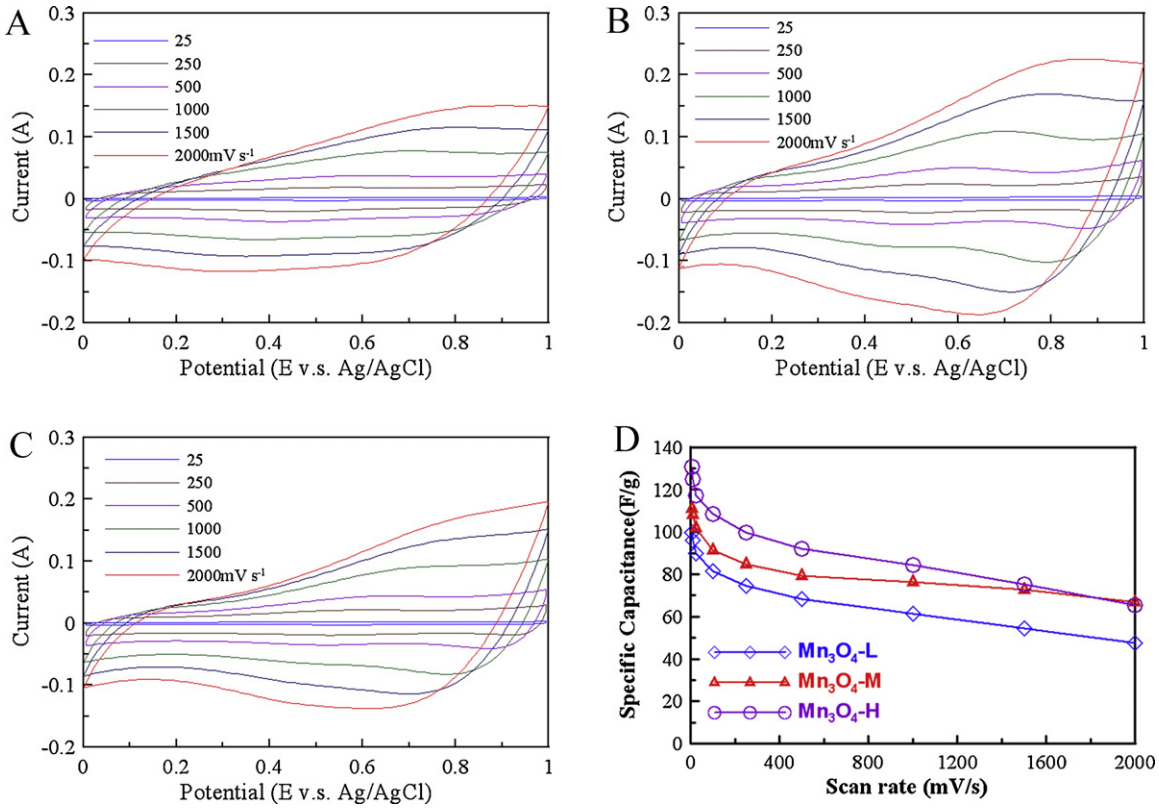

Fig. 8. CV curves of (A) Mn_3O_4-L, (B) Mn_3O_4-M, and (C) Mn_3O_4-H measured in 0.5 M Na_2SO_4 at different scan rates. (D) Dependence of the specific capacitance on the scan rate of CV for (1) Mn_3O_4-L, (2) Mn_3O_4-M, and (3) Mn_3O_4-H.

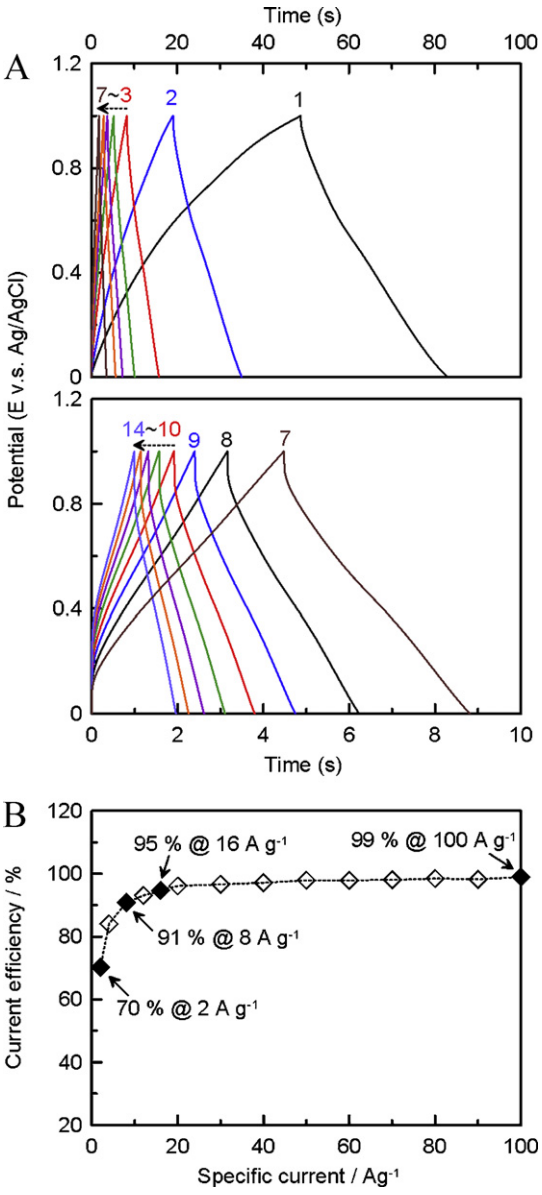

Fig. 9. (A) Chronopotentiograms of Mn_3O_4-H measured at (1) 2, (2) 4, (3) 8, (4) 12, (5) 16, (6) 20, (7) 30, (8) 40, (9) 50, (10) 60, (11) 70, (12) 80, (13) 90, and (14) 100 A g^{-1} and (B) corresponding current efficiency of charge–discharge at various specific currents.

4. Conclusions

We successfully designed Mn_3O_4 nanoparticles with tunable microstructures and high surface area by varying the amount of copolymer for achieving the excellent capacitive performances (e.g., high-power characteristics and impressive capacity retention) for the next generation supercapacitors. This route effectively increases/tunes the specific surface area/pore structure of Mn_3O_4 nanoparticles, enhancing the facility of ion transportation and electrolyte permeation for the high-rate charging/discharging purpose in the supercapacitor application. In general, the higher specific surface area of Mn_3O_4 provides the more electrochemically active sites for the charge storage and delivery. However, the significant formation of mesopores (and certain macropores), indexed by the BJH pore volume, may affect the ion transportation and electrolyte permeation during the process of charge storage/delivery, which becomes the bottleneck step at very high scan rates of CV. The above concepts are applicable to other oxides for enhancing the performances of various electrochemical systems.

Acknowledgements

This work was financially supported by the National Science Council of Taiwan under NSC100-3113-E-006-001 and the boost program from Low Carbon Energy Research Center of National Tsing Hua University.

Appendix A. Supplementary data

Supplementary data associated with this article can be found, in the online version, at doi:10.1016/j.jpowsour.2012.01.121.

References

[1] M. Muthukumar, C.K. Ober, E.L. Thomas, Science 277 (1997) 1225.
[2] G.H. Fredrickson, F.S. Bates, Annu. Rev. Mater. Sci. 26 (1996) 501.
[3] A.V. Blaaderen, R. Ruel, P. Wiltzius, Nature 385 (1997) 321.
[4] M.R. Ghadiri, J.R. Cranja, L.K. Buehler, Nature 369 (1997) 301.
[5] P. Yang, D. Zhao, D.I. Margolese, B.F. Chmelka, G.D. Stucky, Nature 396 (1998) 152.
[6] P. Yang, D. Zhao, D.I. Margolese, B.F. Chmelka, G.D. Stucky, Chem. Mater. 11 (1999) 2813.
[7] D.A. Doshi, A. Gibaud, V. Goletto, M. Lu, H. Gerung, B. Ocko, S.M. Han, C.J. Brinker, J. Am. Chem. Soc. 125 (2003) 11646.
[8] C.W. Wu, T. Ohsuna, M. Kuwabara, K. Kuroda, J. Am. Chem. Soc. 128 (2006) 4544.
[9] S. Yang, X. Zhou, P. Yuan, M. Yu, S. Xie, J. Zou, G.Q. Lu, C. Yu, Angew. Chem. Int. Ed. 46 (2007) 8579.
[10] J. Tang, X. Zhou, D. Zhao, G.Q. Lu, J. Zou, C. Yu, J. Am. Chem. Soc. 129 (2007) 9044.
[11] S. Tominaka, C.W. Wu, T. Momma, K. Kuroda, T. Osaka, Chem. Commun. 25 (2008) 2888.
[12] Y.F. Lee, K.H. Chang, C.C. Hu, Chem. Commun. 47 (2011) 2297.
[13] Y.F. Lee, K.H. Chang, C.C. Hu, Y.H. Lee, J. Mater. Chem. 21 (2011) 14008.
[14] Y.F. Lee, K.H. Chang, C.C. Hu, K.M. Lin, J. Mater. Chem. 20 (2010) 5682.
[15] K.M. Lin, K.H. Chang, C.C. Hu, Y.Y. Li, Electrochim. Acta 54 (2009) 4574.
[16] T. Yamashita, A. Vannice, J. Catal. 161 (1996) 254.
[17] H. Einaga, S. Futamura, J. Catal. 227 (2004) 304.
[18] O. Giraldo, S.L. Brock, W.S. Willis, M. Marquez, S.L. Suib, S. Ching, J. Am. Chem. Soc. 122 (2000) 9330.
[19] S.L. Brock, M.J. Nair, S.L. Suib, T. Ressler, J. Phys. Chem. B 105 (2001) 5404.
[20] Y.F. Shen, R.P. Zerger, R.N. Deguzman, S.L. Suib, L. Mccurdy, D.I. Potter, C.L. Oyoung, Science 206 (1993) 511.
[21] Y. Lvov, B. Munge, O. Giraldo, I. Ichinose, S.L. Suib, J.F. Rusling, Langmuir 16 (2000) 8850.
[22] W.S. Seo, H.H. Jo, K. Lee, B. Kim, S.J. Oh, J.T. Park, Angew. Chem. Int. Ed. 43 (2004) 1115.
[23] C.W. Na, D.S. Han, D.S. Kim, J. Park, Y.T. Jeon, G. Lee, M.H. Jung, Appl. Phys. Lett. 87 (2005) 142504.
[24] M.M. Thackery, A. Dekock, M.H. Rossouw, D. Liles, R. Bittihn, D. Hoge, J. Electrochem. Soc. 139 (1992) 363.
[25] K.S. Park, M.H. Cho, S.H. Park, K.S. Nahm, Y.K. Sun, Y.S. Lee, M. Yoshio, Electrochim. Acta 47 (2002) 2937.
[26] C.C. Hu, T.W. Tsou, Electrochem. Commun. 4 (2002) 105.
[27] J. Junhua, K. Anthony, Electrochim. Acta 47 (2002) 2381.
[28] M. Toupin, T. Brousse, D. Belanger, Chem. Mater. 16 (2004) 3184.
[29] M. Johns, P. Landon, T. Alderson, G.J. Hutchings, Chem. Commun. (2001) 2454.
[30] N. Sakai, Y. Ebina, K. Takada, T. Sasaki, J. Electrochem. Soc. 152 (2005) E384.
[31] D. Im, A. Manthiram, J. Electrochem. Soc. 150 (2003) A68.
[32] T. Ahmad, K.V. Ramanujachary, S.E. Lofland, A.K. Ganguli, J. Mater. Chem. 14 (2004) 3406.
[33] H.Y. Xu, S.L. Xu, X.D. Li, H. Wang, H. Yan, Appl. Surf. Sci. 252 (2006) 4091.
[34] Y.T. Wu, C.C. Hu, Electrochem. Solid State Lett. 8 (2005) A240.
[35] Y.S. Ding, X.F. Shen, S. Gomez, H. Luo, M. Aindow, S.L. Suib, Adv. Funct. Mater. 16 (2006) 549.
[36] S.L. Kuo, N.L. Wu, J. Electrochem. Soc. 153 (2006) A1317.
[37] J.M. Tarascon, M. Armand, Nature 414 (2001) 359.
[38] L. Taberna, S. Mitra, P. Poizot, P. Simon, J.M. Tarascon, Nat. Mater. 5 (2006) 567.
[39] F. Jiao, P.G. Bruce, Adv. Mater. 19 (2007) 657.
[40] K.H. Chang, Y.F. Lee, C.C. Hu, C.I. Chang, C.L. Liu, Y.L. Yang, Chem. Commun. 46 (2010) 7957.
[41] C.C. Hu, Y.T. Wu, K.H. Chang, Chem. Mater. 20 (2008) 2890.
[42] C.C. Hu, C.Y. Hung, K.H. Chang, Y.L. Yang, J. Power Sources 196 (2011) 847.
[43] C.C. Hu, P.Y. Chang, Y.T. Wu, J. Electrochem. Soc. 152 (2005) C723.
[44] D.W. Wang, F. Li, M. Liu, G.Q. Lu, H.M. Cheng, Angew. Chem. Int. Ed. 47 (2008) 373.
[45] F. Ataherian, N.L. Wu, J. Electrochem. Soc. 158 (2011) A422.
[46] Y.H. Chu, C.C. Hu, K.H. Chang, Electrochim. Acta 61 (2012) 124.
[47] S. Komaba, A. Ogata, T. Tsuchikawa, Electrochem. Commun. 10 (2008) 1435.